Journal of Non-Crystalline Solids 500 (2018) 410–416

Contents lists available at ScienceDirect

Journal of Non-Crystalline Solids

journal homepage: www.elsevier.com/locate/jnoncrysol

Solute aggregation in $Ca_{72}Zn_{28}$ metallic glass

Duygu Tahaoğlu, Murat Durandurdu*

Department of Materials Science & Nanotechnology Engineering, Abdullah Gül University, Kayseri 38039, Turkey

ARTICLE INFO

Keywords:
Metallic glass
Segregation
Ca-Zn systems

ABSTRACT

Solidification of the $Ca_{72}Zn_{28}$ melt is achieved by using both the thermal quenching and rapid pressurizing techniques in ab initio molecular dynamics simulations within a generalized gradient approximation. A chemical segregation process is perceived in the $Ca_{72}Zn_{28}$ system and hence the resulting configurations show nanosized glassy domains with different compositions. The structural and mechanical properties of both $Ca_{72}Zn_{28}$ metallic glasses have been probed by using various analyzing methods. Although the mean coordination number of the both models is found to be fairly close to each other, a careful investigation exposes that they have a different short-range order around Zn atoms. It appears that pressurizing significantly affects the environment of Zn atom, suppresses the occurrence of Zn-centered ideal icosahedral polyhedrons and retains the Zn centered tri-capped trigonal prism–like configurations. On the other hand, the impact of pressure on the environment of Ca atoms is found to be not too drastic. The computer-generated models represent slightly different mechanical properties. The model obtained using the rapid pressurizing technique is stiffer than the one produced using the thermal quenching technique.

1. Introduction

Bulk metallic glasses (BMGs) have been drawing attention of researchers for recent few decades since the discovery of non-crystalline metallic structures [1]. Having amorphous arrangements of metal atoms differently from the crystals leads to some attractive mechanical, physical and chemical possessions, such as high strength, corrosion and wear resistance superior to their crystals [2,3]. Their amorphous structures imply the absence of a certain stoichiometry; a great variety of possible compositions in other words, which provides the convenience of manipulation of the material properties [4].

Amorphous alloys, which consist of light metals like titanium, magnesium and especially calcium, are attracting great attentions because of their low density. The advantages of Ca-based materials are to have relatively low cost and favorable strength to density ratios for potential application fields such as aerospace and transportation industries. Yet the Ca-based amorphous alloys can have some drawbacks such as brittleness [5]. Depending on the alloying elements, such a cumbersome can be eliminated and their mechanical properties can be improved [5].

Metallic glasses also come to the forefront as potential materials in the researches of biomedical applications, particularly as promising candidates for biomedical implants [6]. In this regard, Ca, Zn and Mg elements are good choices as being essential elements inherently allowable for humans to fabricate biodegradable materials. In recent years, there have been significant attentions on the development of new bioresorbable implants, especially focused on the ternary metallic glasses of these elements in different composition [4,7,8]. These studies have revealed their suitability for the biodegradable orthopaedic fixation implements when their mechanical properties and densities are considered. In addition, these materials make possible the avoidance of a second removal surgical operation [9,10] because they can corrode in the body by the effects of body fluids. These amorphous materials have lower degradation rates than the conventional crystalline metal alloys, which provide the tissues enough time for healing. The studies conducted by Zberg et al. [11] and Gu et al. [7] have shown that the Mg-Zn-Ca bulk metallic glasses have lower corrosion, more uniform corrosion morphology and more positive cellular reaction compared to pure Mg implants. The appropriateness of Ca based Ca-Mg-Zn bulk metallic glasses for skeletal applications have also been demonstrated in both in vitro studies and it has been shown that no obvious inflammation reaction or animal death have been encountered [8,12] in vivo implantations.

All these literature researches and technological applications of Ca based metallic glasses stimulate our interest in this field. In spite of the existence of deep interest on ternary bulk metallic glasses due to their complementary properties, there is almost no evidence about fabrication, structural and mechanical properties of binary Ca-Zn metallic

* Corresponding author.
E-mail address: murat.durandurdu@agu.edu.tr (M. Durandurdu).

https://doi.org/10.1016/j.jnoncrysol.2018.08.030
Received 21 May 2018; Received in revised form 9 August 2018; Accepted 23 August 2018
Available online 31 August 2018

glass except the experimental and theoretical data reported by Widom et al. [5]. In this work, we achieve $Ca_{72}Zn_{28}$ metallic glasses via two different fabrication procedures by means of ab initio molecular dynamics (AIMD) principles and investigate their properties by using various analyzing methods. Our study allows us to compare the influences of the fabrication techniques on the local structures including the coordination numbers, polyhedral distributions and bonding preferences, which are the determinants of mechanical performance of a material, and to reveal the best fabrication technique for this system. The AIMD method, which was developed by Car and Parrinello [13], is accepted a useful computational approach in spite of the size limitation on the system with a few hundred of atoms because of the computational expense. Nonetheless the AIMD methods are widely used to simulate metallic glasses and to explore their atomic structure and properties in details. In spite of size limitation, they provide data in good agreement with experimental results [4,14,15]. Consequently we feel safe to perform our simulations within this scheme.

2. Computational method

All calculations were performed by using the ab initio molecular dynamics (AIMD) SIESTA package [16]. We built a supercell containing 200 atoms by placing elements randomly with a desired composition (144 Ca atom, 56 Zn atom) and applied the periodic boundary conditions on the supercell. After liquefying the structure at 1000 K for about 100 ps (each MD step is one femtosecond), we run additional 1000 MD steps to collect data for the structural analysis (structure factor, pair distribution functions, Voronoi, bond pair etc.) and to compute mean-square displacement-MDS that was used to determine the liquid character of the system (see Fig. S1). Then two procedures were used to attain amorphous $Ca_{72}Zn_{28}$ as summarized in Fig. 1. The anneal type-of-run (velocity scaling) was used in all steps of modeling metallic glasses in order to equilibrate the system during quenching or pressurizing techniques. In the method I (thermal quenching technique-TQT), the liquid state was stepwise quenched down to the 300 K at a rate of 6.7×10^{12} K/s by balancing the temperature after every 100 K decrease and then the resulting amorphous solid structure at 300 K was relaxed using the conjugant gradient (CG) method. In the method II (rapid pressurizing technique-RPT), a hydrostatic pressure via the Parrinello-Rahman technique was applied on the liquid structure at 1000 K and increased by 5 GPa until it solidified at 20 GPa (At each applied pressure, the system was equilibrated at least 20 ps and additional 1000 MD steps were run to accumulate the data for the structural analyses and MSD calculations). Then the temperature was decreased to 300 K followed by the releasing pressure. The obtained structure was again relaxed by the CG method. All calculations were performed by the diagonalization solution method within the generalized gradient approximation (GGA) of Perdew-Burke-Ernzerhof (PBE) [17]. Norm-conserving pseudopotentials of Troullier and Martins [18] were used. The wave functions were expressed in double zeta polarized (DZP) basis size. The structures were visualized on VESTA [19]. Some of the structural analyses were performed using ISAACS program [20]. The mesh cutoff energy used is 150.0 Ry.

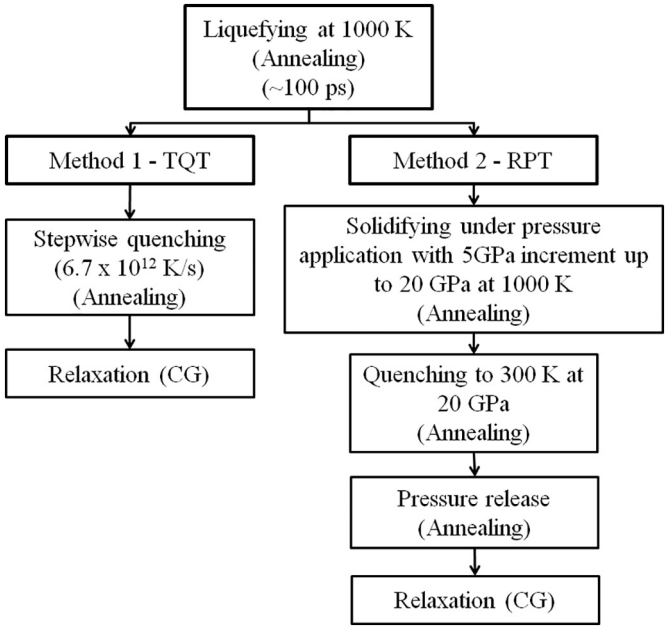

Fig. 1. Schematic representation of the metallic glass production methods used in this study.

The relaxed structures obtained from the TQT and RPT processes were subjected to hydrostatic pressure with a small increment to estimate their energy-volume data. Then the acquired data were used to determine the bulk modulus (B) of the metallic glasses by means of the third order Birch-Murnaghan equation of state [21–23] (Eq. (1))

$$E(V) = E_0 + \frac{9V_0B_0}{16}\left\{\left[\left(\frac{V_0}{V}\right)^{\frac{2}{3}} - 1\right]^3 B_0' + \left[\left(\frac{V_0}{V}\right)^{\frac{2}{3}} - 1\right]^2\left[6 - 4\left(\frac{V_0}{V}\right)^{\frac{2}{3}}\right]\right\} \quad (1)$$

where E is the internal energy, V is the volume, and B' is the pressure derivative of B. The subscript "0" corresponds to the values at equilibrium. According to the energy data, the metallic glass generated by TQT process is found more energetically favorable.

Poisson's ratio (ν) is another important material characteristic and can be used to estimate the other elastic constants. To determine the Poisson's ratio of the metallic glasses, a uniaxial compression was applied for all three axes and six different values are estimated using the following relation:

$$\nu_{ij} = -\frac{\varepsilon_{lateral}}{\varepsilon_{axial}} = -\frac{\Delta L_i/L_i}{\Delta L_j/L_j} \quad (2)$$

$\Delta L_i/L_i$ gives the strain in the direction of load (i-axis) and $\Delta L_j/L_j$ is the strain at right angle to the load (j-axis).

Young's modulus (E), known as the elastic modulus, is a measure of a material's opposition to being deformed elastically (stiffness). It is expressed as the fraction of stress to strain as shown in Eq. (3).

$$E = \frac{\sigma}{\Delta L/L_0} \quad (3)$$

Alternative way to determine the Young's modulus is to benefit from its relation with bulk modulus and Poisson's ratio,

$$E = 3B(1 - 2\upsilon) \quad (4)$$

In order to estimate the shear modulus of the metallic amorphous systems, we used the relation between elastic modulus and Poisson's ratio as represented in Eq. (5).

$$G = \frac{E}{2(1 + \upsilon)} \quad (5)$$

The Vickers hardness of the materials was computed by using the Eq. (6), which is a valid evidence of the linear relationship between hardness and shear modulus observed by Teter [24].

$$H_v = 0.151G \quad (6)$$

where G is the shear modulus.

3. Results and discussion

3.1. Pair distribution functions

Pair correlation function, g(r), is a powerful tool to have

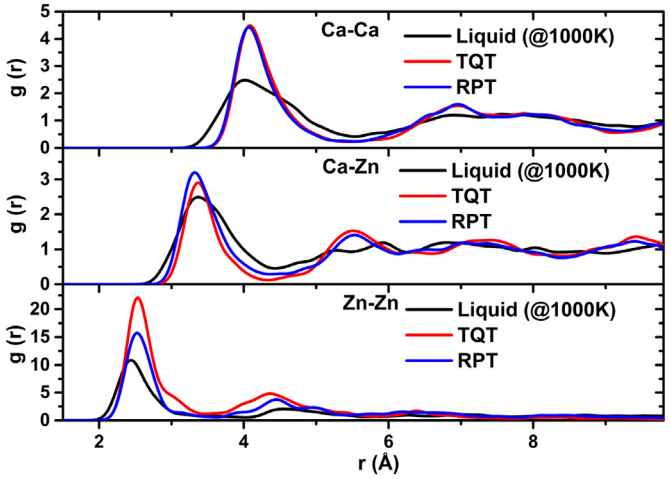

Fig. 2. Pair distribution functions (PDFs) of $Ca_{72}Zn_{28}$ metallic glasses and its liquid state at 1000 K.

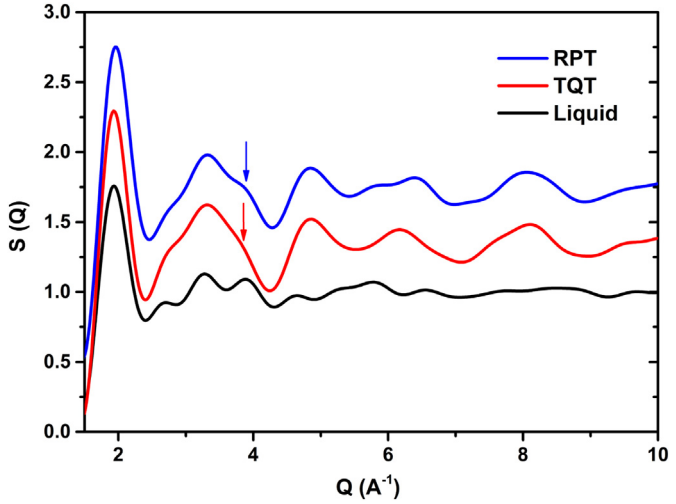

Fig. 3. Calculated structure factors, S(Q), of metallic glasses and the liquid state at 1000 K and zero pressure.

Table 1
The interatomic bond distances between nearest neighbor atoms.

	Liquid state (1000 K)	TQT	RPT	References [25,26] (r_m)
Ca-Zn	3.38	3.36 Å	3.32 Å	3.31 Å
Ca-Ca	4.03	4.09 Å	4.07 Å	3.94 Å
Zn-Zn	2.43	2.52 Å	2.51 Å	2.68 Å

information about the structures at the atomistic level. It gives a statistical view of finding other atoms in a spherical shell around another, which is taken as a center. Fig. 2 gives the pair distribution functions of the resulting metallic glass structures generated by the TQT and RPT processes. It can be clearly seen that the methods used to obtain the metallic glass do not make much difference in the position of all peaks in the pair distribution functions and as understood from Table 1, the bond lengths are fairly close to each other. Yet one can see that the intensity of the Ca-Zn and Zn-Zn correlations is noticeably different in the models. The higher intensity in the Ca-Zn and Zn-Zn correlations means the formation of more Ca-Zn clusters in the RPT model and of more Zn-Zn ones in the TQT model.

The alteration of the interatomic distances during the thermal solidification processes is shown in Fig. S2. The bond lengths (Ca-Ca, Ca-Zn and Zn-Zn) do show some fluctuations during the quenching procedure and hence we are not able to propose a general trend for them. Yet as seen in Table 1, when the bond distances of the TQT model are compared to those of the liquid state, we find that the Ca-Zn bond length is shorten whereas the Zn-Zn and Ca-Ca separations are enlarged. In the RPT process, the application of external pressure leads to the shortening of the Ca-Ca (~12.6%) and Ca-Zn (~1.6%) bond lengths, but an increase in the Zn-Zn distance. The bond distances of the liquid state are not recovered even after full removal of the external pressure at 300 K. Relative to the liquid state, the Ca-Zn bond length is reduced though the Zn-Zn and Ca-Ca separations are increased in the RPT model as well (see Table 1).

It should be noted that the Zn-Zn bond distance is noticeably shorter (about ~6%) than the respective metallic bond length (r_m) and Ca-Ca bond distance is ~3.5% longer than the Ca-Ca metallic bonds (see Table 1).

Perhaps the most important finding in the pair correlation function analysis is that the Zn-Zn correlation does not go to one (expected for amorphous networks) but approaches zero beyond a certain distance for the models. This means the formation of isolated Zn-Zn clusters in both metallic glasses.

In general, it is expected to see the icosahedral short-range ordering (ISRO) in the metallic glasses. The structure factor analysis can be used to find an evidence of the existence of ISRO. Fig. 3 shows the calculated structure factors of the resulting amorphous configurations and the liquid state. As it is specified on the figure, the second peak of the metallic glasses presents a small shoulder on the right hand side, which is an indicator of ISRO [27–29].

3.2. Aggregation of elements

Fig. 4 demonstrates the ball-stick representation of $Ca_{72}Zn_{28}$ systems. In Fig. 4a, the supercell created with randomly distributed Ca and Zn atoms, the initial structure, is shown. In this structure, Zn atoms are distributed almost uniformly among the Ca atoms. In Fig. 4b and c, the final metallic glasses are represented. As it can be clearly seen from the figure, Zn atoms aggregate and create a clear phase separation and hence the formation of Zn-based nano-sized glassy regions.

To determine whether the initial structure has an effect on the phase separation, we used a tetrahedrally coordinated configuration as a starting structure and liquefied it. After 40 ps MD at 1000 K, we again observed clear phase separations as shown in Fig. S3, indicating that initial structure has no impact on the aggregation process.

3.3. Coordination numbers

Total and partial coordination numbers are estimated by using the first minimum of the correlations functions as a cutoff. Table 2 gives the average and partial coordination numbers. The average coordination numbers of two metallic glasses are found as ~12.86 and ~13.00 for the TQT and RPT configurations, respectively. More elaborative information about the distributions of clusters with different coordination numbers is given in Fig. 5. We witness that RPT method leads to a lower coordination for Zn atoms and a higher coordination for Ca atoms compared to the TQT model. The coordination numbers of atoms are also defined with the statistics of the Voronoi analysis, which will be interpreted further on the following pages. The results are given in Table S1 and S2. One can see that the development of more Ca-Zn coordination in the RPT model and of more Zn-Zn coordination in the TQT model as suggested in the pair distribution investigation. A careful analysis further reveals that the low coordinated Zn atoms have more Ca neighbors while the high coordinated ones have more Zn neighbors. This might be due to the atomic radius of these atoms. Ca atom has larger radius than Zn atom and hence Zn atoms form less coordination with Ca atoms. In the Ca rich regions, Ca contains very few Zn atoms as neighbors, which can be also regarded as an indication of a phase

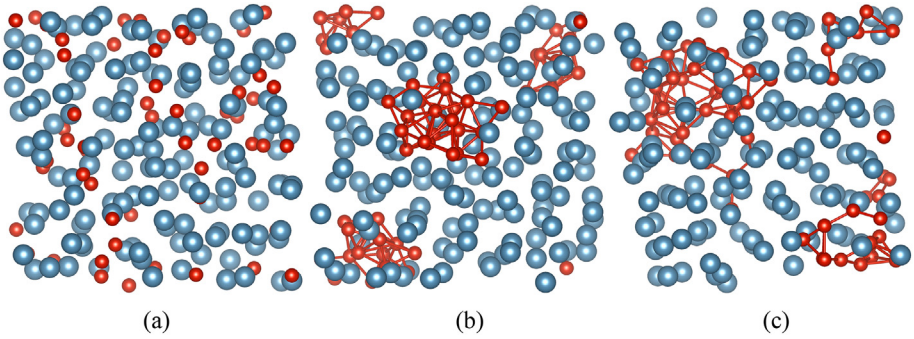

Fig. 4. Structure snapshots of (a) randomly created initial structure, (b) resulting metallic glass from TQT and (c) the metallic glass obtained from RPT.

Table 2
Partial and total coordination numbers around Ca, and Zn atoms in the liquid and final metallic glasses, according to the Voronoi tessellation.

Coordination number	At 1000 K	TQT	RPT
N_{Ca-Ca}	11	12.13	11.92
N_{Ca-Zn}	2	1.66	2.15
N_{Ca}	13	13.79	14.07
N_{Zn-Zn}	3.43	6.21	4.39
N_{Zn-Ca}	5.86	4.27	5.54
N_{Zn}	9.29	10.48	9.93

separation.

The DTF calculations also enable us to monitor the structural modifications during the solidification processes besides the analysis of the final amorphous structures. Coordination profiles during the TQT and RPT processes are shown in Fig. S4. While a slight increase occurs in the average coordination number of Ca atoms as 0.2, the mean coordination number of Zn atoms increases by 1.2 with the temperature decrease in the TQT process. The RPT method, on the other hand, leads to the formation of higher coordinated Ca atoms and lower coordinated Zn atoms compared to the TQT method.

3.4. Bond pair (Honeycutt-Anderson) analysis

Unlike crystals, amorphous materials do not have a long-range order. Therefore, to identify their local structure characteristics, we have to investigate the atomic arrangements in short range order (SRO) by using some analyzing methods such as bond pair analysis and Voronoi cluster identification.

Bonding types were represented by Honeycutt and Anderson's [30] bond pair classification of atomic clusters. In the analysis, four numbers (i, j, k, l) are used to represent the bonding types. The first number indicates whether two atoms in the pair of interest are bonded to each other ($i = 1$) or not ($i = 2$). Second (j) and third (k) numbers give the number of common neighbor atoms and number of bonds among them, respectively. The forth number (l) is a special number to designate the bonds among the neighbor atoms.

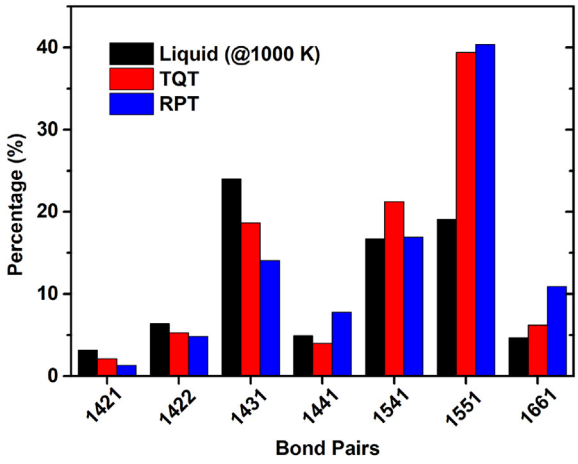

Fig. 6. Distribution of the relative bond pair numbers of liquid state and resulting metallic glasses in TQT and RPT processes.

Fig. 6 shows the various bond pair types existed in the liquid states and the resulting metallic glasses. The bond pairs having a percentage < 2% are not represented in the figure. From Fig. 6, it can be clearly seen that 1551, and 1541, corresponding to icosahedral ordering and icosahedral defects, are the most dominant pairs having a total frequency of ~61% and ~57% for the TQT and RPT models, respectively. The 1431 type of bonding, which is corresponding to tetrahedral clusters, appears as a second favorable bond pair type in both resulting structures with around 18.7% (TQT model) and 14.1% (RPT model), followed by bcc type cluster that is represented by 1661 and

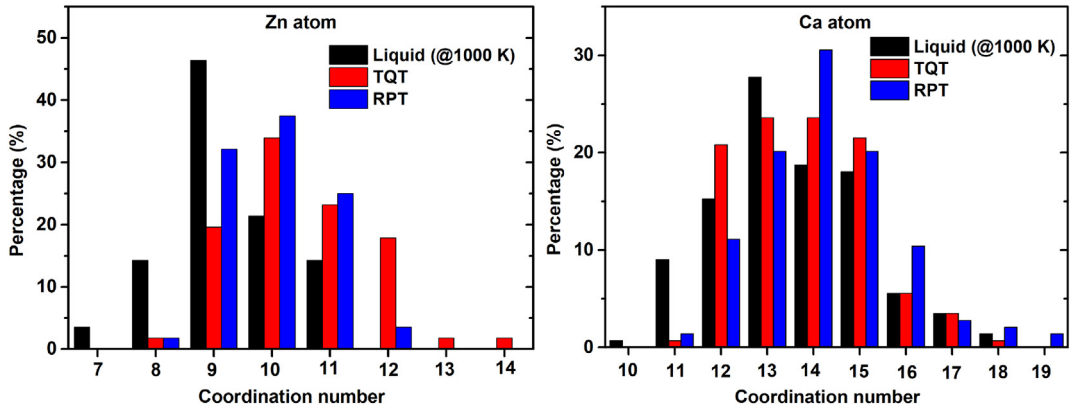

Fig. 5. Coordination distributions of Zn and Ca atoms.

Table 3
Zn-centered voronoi cluster distributions in liquid $Ca_{72}Zn_{28}$ and the metallic glass structures.

Type of Voronoi polyhedra	% at 1000 K	MG from TQT	MG from RPT
⟨0, 4, 4, 0⟩	**12.5**	1.79	1.79
⟨0, 3, 6, 0⟩	**32.14**	**17.86**	**30.36**
⟨0, 2, 8, 0⟩	7.14	**19.64**	8.93
⟨0, 4, 4, 1⟩	5.35	1.78	1.78
⟨0, 3, 6, 1⟩	8.93	**10.71**	**25**
⟨0, 2, 8, 1⟩	7.14	**19.64**	**17.86**
⟨1, 3, 3, 2⟩	7.14	0	0
⟨0, 3, 6, 2⟩	5.36	1.78	0
⟨0, 0, 12, 0⟩	0	**10.71**	0
⟨0, 2, 8, 2⟩	0	3.57	1.79
⟨0, 4, 4, 3⟩	0	0	3.57

1441. The hcp (1421 and 1422) and fcc (1421) types of bonding form in the models with a very small frequency. Although the trend in bond pairs during the solidification process (we see a significant increase of ~20% in icosahedral type of bonding) are more or less similar, more bcc and less tetrahedral and icosahedral-defect types of bond pairs form in the RPT models relative to the TQT model. (See Fig. 6).

3.5. Voronoi clusters

In order to further clarify the short-range order and classify the possible types of clusters formed in the models, we use the Voronoi tessellation method [2,31]. The indexes n_i in $\langle n_3, n_4, n_5, n_6, \ldots\rangle$ represents the i-edged faces of the Voronoi polyhedron and total coordination number equals to $\sum_i n_i$. This definition of cluster types and coordination number is very sensitive to the preference of the cutoff value for the interatomic distances.

Due to the segregation of atoms of two species and non-homogeneity of the structure, it will be proper to show the Voronoi clusters as solute and solvent centered separately to have a better insight for whole system. The distributions of Ca- and Zn-centered Voronoi clusters are given in Table 3 and Table 4.

These tables reveal the differences between two metallic glasses. The TQT model has the Z11 ⟨0, 2, 8, 1⟩. Z10 ⟨0, 2, 8, 0⟩ and Z9 ⟨0, 3, 6, 0⟩ Zn-centered polyhedra with highest frequencies, which correspond to defective icosahedra-like, bi-capped square archimedean antiprism and tri-capped trigonal prism, respectively. The ideal icosahedral cluster (Z12 ⟨0, 0, 12, 0⟩), which is the only Kasper polyhedra for Zn-centered clusters except the Z12 ⟨0, 2, 8, 2⟩ with a low frequency, also have a non-negligible frequency with ~10.7%. On the other hand, we do not see any ideal icosahedron (Z12 ⟨0, 0, 12, 0⟩) for the Zn-centered clusters in the RPT model, indicating that pressure suppresses its formation. For this amorphous configuration, the Z9 ⟨0, 3, 6, 0⟩, Z10 ⟨0, 3, 6, 1⟩ and Z11 ⟨0, 2, 8, 1⟩ Voronoi indexed polyhedrons become prominent one with ~30.4%, 25% and 17.9% population, respectively.

Table 4
Ca-centered voronoi cluster distributions in liquid $Ca_{72}Zn_{28}$ and the metallic glass structures.

Type of Voronoi polyhedra	Liquid (at 1000 K)	TQT	RPT
⟨0, 2, 8, 2⟩	8.33	5.56	4.17
⟨0, 1, 10, 2⟩	4.86	**10.42**	**12.5**
⟨0, 3, 6, 3⟩	4.86	4.86	0
⟨0, 2, 8, 3⟩	4.86	3.48	0
⟨0, 1, 10, 3⟩	2.78	8.33	5.56
⟨0, 3, 6, 4⟩	9.03	6.25	3.47
⟨0, 2, 8, 4⟩	6.25	**10.42**	**14.58**
⟨0, 1, 10, 4⟩	4.86	6.94	6.25
⟨0, 2, 8, 5⟩	3.47	4.86	2.78
⟨0, 0, 12, 0⟩	0	**9.03**	**8.33**
⟨0, 0, 12, 2⟩	0	2.08	4.17

From the Table, one can see that pressure favors the formation of Z10 ⟨0, 3, 6, 1⟩ and Z11 ⟨0, 2, 8, 1⟩ type clusters. The Z9 ⟨0, 3, 6, 0⟩ – bi-capped square archimedean antiprism-type of clusters are the characteristic polyhedra with > 30% in the liquid state and it does not show a substantial change in the RPT process while fell by almost half in the TQT model. This finding implies that pressure somehow preserves Z9 ⟨0, 3, 6, 0⟩ type cluster.

Ca-centered clusters have higher number of distinct polyhedron types. The Z13 ⟨0, 1, 10, 2⟩ distorted icosahedra and Z14 ⟨0, 2, 8, 4⟩ types of polyhedra are found to be as the most salient cluster types for both metallic glasses with > 10% population for each. Ca-centered perfect icosahedrons do not exist in the liquid state. Yet during both solidification processes, they form with a frequency of 9.02% (TQT-model) and 8.33% (RPT-model). These findings suggest that the fabrication method has almost no influence on the environment of Ca atoms.

In order to have an idea about the medium range order in the metallic glasses, the construction of the polyhedral clusters has been examined. Fig. 7 shows the selected regions, which are rich in the solute concentration due to the atomic segregation. In the metallic glasses, the solute centered ⟨0, 2, 8, 0⟩ and ⟨0, 2, 8, 1⟩ clusters are found to be together connected by their centers while the ⟨0, 3, 6, 0⟩ and ⟨0, 3, 6, 1⟩ clusters favor to be in the same part of the Zn rich region. See Figs. S6–S7 for the distribution of most common clusters.

3.6. Mechanical properties

We have found the metallic glass densities as 1.87 and 1.91 g/cm^3 for the products of the TQT and RPT models, respectively, whose values are very similar to the non-porous bone (~1.9 g/cm^3) [6]. These results are in a good agreement with the Ca-based BMGs, which are known to have low densities of ~2.0 g/cm^3 [32]. The experimental density value of the $Ca_{72}Zn_{28}$ metallic glass is also given as 2.23 g/cm^3 by Widom et al. [5].

Ca-based metallic glasses are identified to have low Young's (~20–35 GPa) and shear modulus (~8–15 GPa) among other metallic glasses [32]. All calculated mechanical properties of final $Ca_{72}Zn_{28}$ metallic glass structures are given in Table 5. Our results are in the lower limit of elastic and shear moduli with values of 18.40–23.53 GPa and 6.85–8.89 GPa, respectively [5,33,34]. Ductility of the metallic glasses is correlated with their shear and bulk moduli. Ductile metallic glasses have been found to have a higher bulk modulus and a lower shear modulus. For metallic glasses, if the ratio G/B is bigger than 0.41–0.43 (or, equivalently, with ν < 0.31–0.32) then the materials are brittle [35]. The ratio G/B is equal to 0.34 for the TQT model and 0.4 for the RPT configuration and ν is equal to 0.34 for the TQT model and 0.32 for the RPT configuration. Note that the values estimated for the RPT model are so close to the critical values. Nonetheless both models are ductile but the TQT model shows more ductility than the RPT model. Widom et al. [5] have also experimentally shown that $Ca_{72}Zn_{28}$ metallic glass is a ductile alloy.

4. Conclusions

In this article we report our results on structural and mechanical properties of the binary $Ca_{72}Zn_{28}$ metallic glass and the effect of fabrication methods on its material characteristics. Both structures show the phase separation of Ca and Zn atoms and exhibit nano-sized glassy regions with different composition. Although Zn region in the metallic glass of TQT process is found to be higher coordinated relative to the other metallic glass, the RPT process yields a higher mean coordination number in general.

The icosahedral ordering shows an increase by about 20% of total during the solidification processes compared to the liquid state. 1551 and 1541 bond pairs corresponding to the icosahedral arrangement are the most dominant type of bonding in the amorphous network with a fraction of around 60%. The differences between the local structures

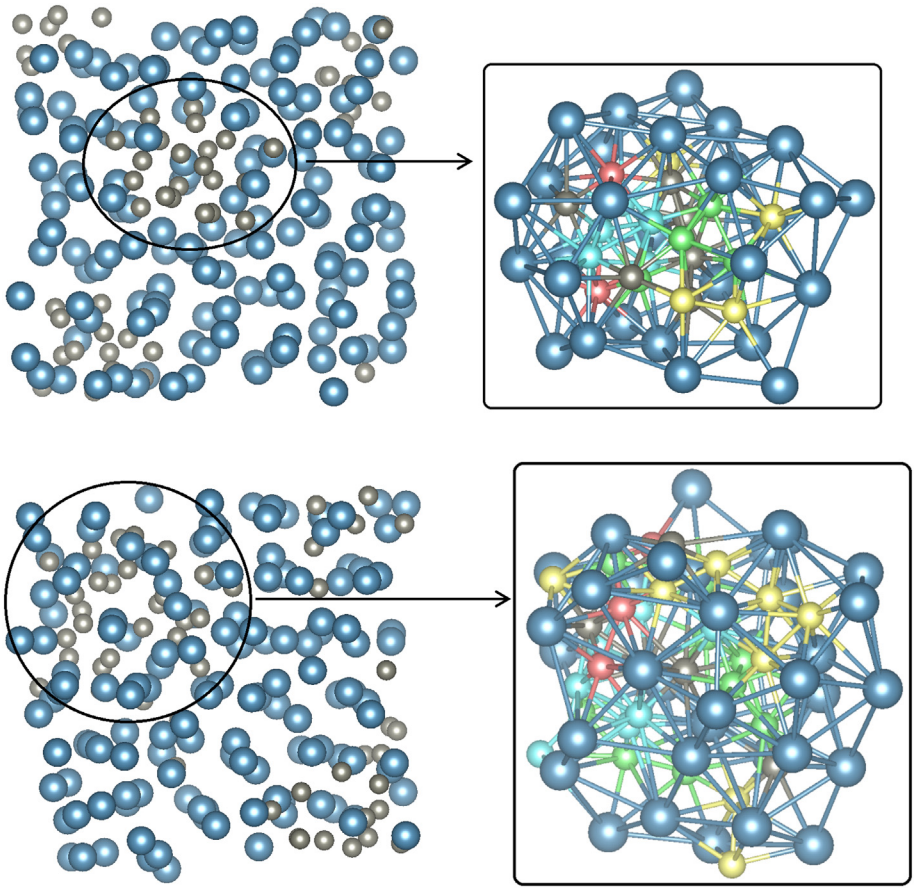

Fig. 7. Configurations of Zn atoms in the selected regions of the metallic glasses simulated by TQT (above) and RPT (below) processes (Yellow: Zn atoms in the center of ⟨0, 3, 6, 0⟩ polyhedron, Green: Zn atoms in the centre of ⟨0, 3, 6, 1⟩ polyhedron, Pink: Zn atoms in the center of ⟨0, 2, 8, 0⟩ polyhedron, Light blue: Zn atoms in the center of ⟨0, 2, 8, 1⟩ polyhedron, Grey: Other Zn atoms in the center of polyhedron having very small percentages). (For interpretation of the references to colour in this figure legend, the reader is referred to the web version of this article.)

Table 5
Mechanical characteristics of $Ca_{72}Zn_{28}$ metallic glasses.

	TQT	RPT	$Ca_{65}Mg_{15}Zn_{20}$	Ca_3Zn
Bulk modulus (B) [GPa]	19.66	22.16	23[33]	21.5[5]
Poisson's ratio (υ)	0.344	0.323	0.306[33]	0.37[5]
Young's modulus (E) [GPa]	18.40	23.53	26.42[33]	–
Shear modulus (G) [GPa]	6.85	8.89	10.12[33]	6.3[5]
Hardness (H_v) [GPa]	1.03	1.34	1.42[34]	–
G/B	0.35	0.40	–	–

have more clearly revealed from the Voronoi analysis. Zn-centered Z10 ⟨0, 2, 8, 0⟩ and Z11 ⟨0, 2, 8, 1⟩ clusters appear as the most predominant types followed by Z9 ⟨0, 3, 6, 0⟩. On the other hand, Z9 ⟨0, 3, 6, 0⟩ and Z10 ⟨0, 3, 6, 1⟩ polyhedron types are the most favorable clusters in the RPT process. Surprisingly, Zn centered Z12 ⟨0, 0, 12, 0⟩ – perfect icosahedral arrangements are only observed in the model generated by the TQT process, suggesting that pressure suppresses the formation of the perfect icosahedral polyhedron. Ca-centered polyhedron types show more similar distributions in both models. The Z13 ⟨0, 1, 10, 2⟩ and Z14 ⟨0, 2, 8, 4⟩ polyhedra have the most dominate ones.

We find that the mechanical properties slightly depend on the production method. The RPT method yields stiffer $Ca_{72}Zn_{28}$ metallic glass than the TQT process. The mechanical properties estimated are in the range of expected values for Ca-based metallic glasses.

Acknowledgements

This is work was supported by the Abdullah Gül University Support Foundation. The calculations were partially run on TÜBİTAK ULAKBİM, High Performance and Grid Computing Center (TRUBA resources) and the High Performance Computer Center at Abdullah Gül University.

Appendix A. Supplementary data

Mean square displacement, variation in bond lengths throughout the processes, different initial structure and phase separation, average coordination numbers during the processes, detailed tables and figures of coordination and Voronoi analyses results. Supplementary data to this article can be found online at https://doi.org/10.1016/j.jnoncrysol.2018.08.030.

References

[1] W. Klement Jun, R.H. Willens, P.O.L. Duwez, Nature 187 (1960) 869.
[2] H.W. Sheng, W.K. Luo, F.M. Alamgir, J.M. Bai, E. Ma, Nature 439 (2006) 419.
[3] C.C. Yu, C.M. Lee, J.P. Chu, J.E. Greene, P.K. Liaw, Appl. Mater. 4 (2016) 116101.
[4] A. Gulenko, L.F. Chungong, J.H. Gao, I. Todd, A.C. Hannon, R.A. Martin, J.K. Christie, Phys. Chem. Chem. Phys. 19 (2017) 8504.
[5] M. Widom, B. Sauerwine, A.M. Cheung, S.J. Poon, P. Tong, D. Louca, G.J. Shiflet, Phys. Rev. B 85 (2011) 054206.
[6] K. Saksl, et al., J. Alloys Compd. 725 (2017) 916.
[7] X.N. Gu, Y.F. Zheng, S.P. Zhong, T.F. Xi, J.Q. Wang, W.H. Wang, Biomaterials 31 (2010) 1093.
[8] Y.B. Wang, X.H. Xie, H.F. Li, X.L. Wang, M.Z. Zhao, E.W. Zhang, Y.J. Bai, Y.F. Zheng, L. Qin, Acta Biomater. 7 (2011) 3196.
[9] H.F. Li, Y.F. Zheng, Acta Biomater. 36 (2016) 1.
[10] O.N. Senkov, J.M. Scott, J. Non-Cryst. Solids 351 (2005) 3087.
[11] B. Zberg, P.J. Uggowitzer, J.F. Loffler, Nat. Mater. 8 (2009) 887.
[12] X.H. Xie, X.L. Wang, Y.B. Wang, G. Zhang, Y.X. He, Y.F. Zheng, L. Qin, Bone 47 (2010) S425.
[13] R. Car, M. Parrinello, Phys. Rev. Lett. 55 (1985) 2471.
[14] H.Z. Fang, X. Hui, G.L. Chen, R. Ottking, Y.H. Liu, J.A. Schaefer, Z.K. Liu, Comput. Mater. Sci. 43 (2008) 1123.
[15] W.Y. Wang, H.Z. Fang, S.L. Shang, H. Zhang, Y. Wang, X. Hui, S. Mathaudhu, Z.K. Liu, Physica B 406 (2011) 3089.
[16] J.M. Soler, E. Artacho, J.D. Gale, A. Garcia, J. Junquera, P. Ordejon, D. Sanchez-Portal, J. Phys. Condens. Mat. 14 (2002) 2745.
[17] J.P. Perdew, K. Burke, M. Ernzerhof, Physical Review Letters, 77 (1996), p. 3865.
[18] N. Troullier, J.L. Martins, Phys. Rev. B 43 (1991) 1993.
[19] K. Momma, F. Izumi, J. Appl. Crystallogr. 44 (2011) 1272.

[20] S. Le Roux, V. Petkov, J. Appl. Crystallogr. 43 (2010) 181.
[21] F. Birch, Phys. Rev. 71 (1947) 809.
[22] M.F. D., Am. J. Math. 59 (1937) 235.
[23] M.F. D., PNAS 30 (1944) 244.
[24] D.M. Teter, MRS Bull. 23 (1998) 22.
[25] B. Cordero, V. Gomez, A.E. Platero-Prats, M. Reves, J. Echeverria, E. Cremades, F. Barragan, S. Alvarez, Dalton T 21 (2008) 2832.
[26] O.N. Senkov, D.B. Miracle, E.R. Barney, A.C. Hannon, Y.Q. Cheng, E. Ma, Phys. Rev. B 82 (2010) 104206.
[27] S. Sachdev, D.R. Nelson, Phys. Rev. Lett. 53 (1984) 1947.
[28] K.F. Kelton, G.W. Lee, A.K. Gangopadhyay, R.W. Hyers, T.J. Rathz, J.R. Rogers, M.B. Robinson, D.S. Robinson, Phys. Rev. Lett. 90 (2003) 195504.
[29] N.A. Mauro, et al., Phys. Rev. B 83 (2011) 184109.
[30] J.D. Honeycutt, H.C. Andersen, J. Phys. Chem. US 91 (1987) 4950.
[31] J.L. Finney, Proc. R. Soc. Lond. A 319 (1970) 479.
[32] O.N. Senkov, D.B. Miracle, V. Keppens, P.K. Liaw, Metall. Mater. Trans. A 39A (2008) 1888.
[33] Z.Y. Zhang, V. Keppens, O.N. Senkov, D.B. Miracle, Mat. Sci. Eng. A Struct. 471 (2007) 151.
[34] G. Wang, P.K. Liaw, O.N. Senkov, D.B. Miracle, M.L. Morrison, Adv. Eng. Mater. 11 (2009) 27.
[35] J.J. Lewandowski, W.H. Wang, A.L. Greer, Philos. Mag. Lett. 85 (2005) 77.